Multistate histogram-free reweighting for vapor-liquid coexistence calculations of non-simulated force field parameters

Richard A. Messerly,[*,†] Mohammad S. Barhaghi,[‡] Jeffrey J. Potoff,[‡] and Michael R. Shirts[¶]

†Thermodynamics Research Center, National Institute of Standards and Technology, Boulder, Colorado, 80305, United States

‡Department of Chemical Engineering and Materials Science, Wayne State University, Detroit, Michigan 48202, United States

¶Department of Chemical and Biological Engineering, University of Colorado, Boulder, Colorado, 80309, United States

E-mail: richard.messerly@nist.gov

Abstract

1 Introduction

A key use of molecular simulation is the ability to accurately and efficiently estimate vapor-liquid coexistence properties, i.e., saturated liquid density ($\rho_{\text{liq}}^{\text{sat}}$), saturated vapor density ($\rho_{\text{vap}}^{\text{sat}}$), saturated vapor pressures ($P_{\text{vap}}^{\text{sat}}$), and enthalpy of vaporization (ΔH_{v}). The accuracy of coexistence estimates depends on the underlying molecular model (a.k.a., force field, potential model, or Hamiltonian) while the computational efficiency depends primarily on the simulation methods, software, and hardware.

Several simulation approaches exist for computing vapor-liquid coexistence properties.[1] These include Gibbs Ensemble Monte Carlo (GEMC), two-phase molecular dynamics (2ϕMD),[2] isothermal-isochoric integration (ITIC),[3] and Grand Canonical Monte Carlo coupled with histogram reweighting (GCMC-HR). Although the development of accurate force fields has been greatly enabled by the improved efficiency of these methods, parameterization of non-bonded interactions with vapor-liquid coexistence calculations over a wide range of temperatures remains an arduous and time-consuming task.[4–8]

The primary purpose of this study is to reduce the computational cost of non-bonded parameterization by implementing the Multistate Bennett Acceptance Ratio (MBAR),[9,10] which is a histogram-free reweighting schema. The proposed GCMC-MBAR method is identical to the traditional GCMC-HR approach except that it uses MBAR to reweight configurations rather than reweighting histograms. The benefit of this simple modification is that GCMC-MBAR can estimate coexistence properties for non-bonded parameter sets that have not been simulated directly.

Although GCMC-HR is a standard approach for computing vapor-liquid coexistence, HR has also been applied to GEMC simulations (GEMC-HR).[11] Therefore, while the present

study presents how MBAR can be applied to GCMC simulations, an analogous GEMC-MBAR approach is worth investigating in future work.

In similar studies, Messerly et al. demonstrate how to combine MBAR with ITIC (MBAR-ITIC) to optimize Mie λ-6 (generalized Lennard-Jones) potentials.[12,13] For MBAR-ITIC, a series of NVT simulations along an isotherm and isochores are performed with a "reference" force field (θ_{ref}). MBAR computes the internal energy (U) and pressure (P) (or compressibility factor, Z) for each $T - \rho$ state point with a non-simulated ("rerun") force field (θ_{rr}). ITIC then converts the U and P values into vapor-liquid coexistence properties.[3,14]

The results from Messerly et al. demonstrate that MBAR-ITIC is most reliable in the local domain, i.e., for parameter sets near the "reference" parameter set from which configurations are sampled.[12] Furthermore, MBAR-ITIC performs best for changes in the non-bonded well-depth parameter (ϵ) while it performs significantly worse for large changes in the non-bonded size and repulsive parameters (σ and λ, respectively). This is typically referred to as poor "overlap" and can be quantified by the "number of effective snapshots" ($K_{\text{snaps}}^{\text{eff}}$), which is essentially the number of non-negligible samples that contribute to the estimated ensemble averages. Poor overlap (low $K_{\text{snaps}}^{\text{eff}}$) is especially problematic for ITIC as a large number of snapshots is needed to obtain precise estimates of P in the liquid phase, which are essential to obtain reasonable values of $\rho_{\text{liq}}^{\text{sat}}$.

Our initial hypothesis was that GCMC-MBAR should have better overlap over the non-bonded parameter space than what was observed for MBAR-ITIC. There are two main reasons for this hypothesis/aspiration. First, as opposed to the fixed density NVT simulations used in ITIC, the fluctuating density of a GCMC simulation produces a wider range of configurations and energies. Second, ITIC requires precise U and P calculations in the supercritical and liquid phase, which necessitates larger box sizes (and, thereby, more molecules) than those typically utilized with GCMC. By utilizing fewer molecules,

GCMC simulations experience larger energy fluctuations (on a percent basis) which improves the overlap between states. We also hypothesized that the impact of poor overlap would be less severe compared to ITIC, where poor overlap leads to sporadic and nonsensical coexistence estimates.

The method outlined in this study is similar in spirit to "Hamiltonian scaling" (HS), which has been applied to both GEMC[15] and GCMC simulations.[1,16–18] The HS approach samples from multiple force fields (Hamiltonians) in a single simulation according to a weighted sampling probability. Vapor-liquid coexistence curves for each force field are estimated post-simulation by reweighting the configurations accordingly. For the Grand Canonical Monte Carlo implementation of Hamiltonian scaling (HS-GCMC), μ and T are not stationary during the simulation, rather the current value of μ and T depends on which force field is being sampled. Despite HS-GCMC proving to be a powerful tool to optimize force field parameters,[1,16–18] it has yet to gain widespread popularity. This is likely due to the added complexity of both the simulation protocol and the histogram post-processing. Also, HS requires that a decision be made *a priori* regarding which force fields are to be tested. By contrast, MBAR does not require any modification of the simulation procedure, the post-processing is essentially unchanged, and the non-bonded parameter sets need not be selected prior to the simulations.

The outline for this study is the following. Section 2 provides details regarding the force fields, simulation set-up, and post-simulation analysis with MBAR. Section 3 provides a comparison of GCMC-MBAR and GCMC-HR as well as various applications of GCMC-MBAR for force field parameterization. Section 4 discusses some limitations and provides recommendations for future work. Section 5 presents the primary conclusions.

2 Methods

2.1 Force fields

The force fields utilized in this study are Transferable Potentials for Phase Equilibria (TraPPE-UA, also referred to simply as TraPPE[4,20,21]), Mie Potentials for Phase Equilibria (MiPPE),[6,22] and Nath, Escobedo, and de Pablo revised (NERD). Each force field adopts a united-atom (UA) representation, where non-polar hydrogens are not modeled explicitly. The non-bonded potential is of the generalized Lennard-Jones (Mie λ-6) form.

The bond lengths for the TraPPE, MiPPE, and NERD force fields are 0.154 nm for all compounds studied. The same angle and dihedral potentials are used for each force field, with the exception of the NERD CH_i-CH-CH_j equilibrium bond angle. Angular bending interactions are evaluated using a harmonic potential:

$$u^{\text{bend}} = \frac{k_\theta}{2} (\theta - \theta_0)^2 \qquad (1)$$

where u^{bend} is the bending energy, θ is the instantaneous bond angle, θ_0 is the equilibrium bond angle (see Table 1), and k_θ is the harmonic force constant with $k_\theta/k_{\text{B}} = 62500 \, \text{K/rad}^2$ for all bonding angles, where k_{B} is the Boltzmann constant.

Table 1: Equilibrium bond angles (θ_0).[20] CH_i and CH_j represent CH_3, CH_2, CH, or C sites.

Bending sites	θ_0 (degrees)
CH_i-CH_2-CH_j	114.0
CH_i-CH-CH_j	112.0
CH_i-CH-CH_j, NERD	109.5
CH_i-C-CH_j	109.5

Dihedral torsional interactions are determined using a cosine series:

$$u^{\text{tors}} = c_0 + c_1[1 + \cos\phi] + c_2[1 - \cos 2\phi] + c_3[1 + \cos 3\phi] \tag{2}$$

where u^{tors} is the torsional energy, ϕ is the dihedral angle and c_n are the Fourier constants listed in Table 2.

Table 2: Fourier constants (c_n/k_{B}) in units of K.[20] CH_i and CH_j represent CH_3, CH_2, CH, or C sites.

Torsion sites	c_0/k_{B}	c_1/k_{B}	c_2/k_{B}	c_3/k_{B}
CH_i-CH_2-CH_2-CH_j	0.0	355.03	-68.19	791.32
CH_i-CH_2-CH-CH_j	-251.06	428.73	-111.85	441.27
CH_i-CH_2-C-CH_j	0.0	0.0	0.0	461.29
CH_i-CH-CH-CH_j	-251.06	428.73	-111.85	441.27

Non-bonded interactions between sites located in two different molecules or separated by more than three bonds within the same molecule are calculated using a Mie λ-6 potential (of which the Lennard-Jones, LJ, 12-6 is a subclass):

$$u^{\text{nb}}(\epsilon, \sigma, \lambda; r) = \left(\frac{\lambda}{\lambda - 6}\right)\left(\frac{\lambda}{6}\right)^{\frac{6}{\lambda-6}} \epsilon \left[\left(\frac{\sigma}{r}\right)^{\lambda} - \left(\frac{\sigma}{r}\right)^6\right] \tag{3}$$

where u^{nb} is the non-bonded energy, σ is the distance (r) where $u^{\text{nb}} = 0$, $-\epsilon$ is the energy of the potential at the minimum $\left(\text{i.e., } u^{\text{nb}} = -\epsilon \text{ and } \frac{\partial u^{\text{nb}}}{\partial r} = 0 \text{ for } r = r_{\min}\right)$, and λ is the repulsive exponent.

The non-bonded Mie λ-6 force field parameters for TraPPE, MiPPE, and NERD are provided in Table 3. MiPPE reports a "generalized" (MiPPE-gen) and "short/long" (MiPPE-SL) CH and C parameter set. The "short" and "long" parameters are implemented when the number of carbons in the backbone is ≤ 4 and > 4, respectively. Also note that the NERD force field has several different parameter sets for CH_3 sites.

Table 3: Non-bonded (intermolecular) parameters for TraPPE,[4,20] MiPPE,[6,22] and NERD.[23]

United-atom	ϵ/k_B (K)	σ (nm)	λ
TraPPE			
CH_3	98	0.375	12
CH_2	46	0.395	12
CH	10	0.468	12
C	0.5	0.640	12
MiPPE			
CH_3	121.25	0.3783	16
CH_2	61	0.399	16
CH, gen.	15	0.46	16
C, gen.	1.2	0.61	16
CH, short	15	0.47	16
C, short	1.45	0.61	16
CH, long	14	0.47	16
C, long	1.2	0.62	16
NERD			
CH_3	104.00	0.3910	12
CH_3 (2-methylpropane)	78.23	0.3880	12
CH_3 (2,2-dimethylpropane)	74.50	0.3910	12
CH_3 (methyl side chain)	70.00	0.3850	12
CH_2	45.80	0.3930	12
CH	39.70	0.3850	12
C	17.00	0.3910	12

Non-bonded parameters between two different site types (i.e., cross-interactions) are determined using Lorentz-Berthelot combining rules[24] for ϵ and σ and an arithmetic mean for the repulsive exponent λ (as recommended in Reference 6):

$$\epsilon_{ij} = \sqrt{\epsilon_{ii}\epsilon_{jj}} \tag{4}$$

$$\sigma_{ij} = \frac{\sigma_{ii} + \sigma_{jj}}{2} \tag{5}$$

$$\lambda_{ij} = \frac{\lambda_{ii} + \lambda_{jj}}{2} \tag{6}$$

where the ij subscript refers to cross-interactions and the subscripts ii and jj refer to same-site interactions.

2.2   Simulation set-up

The majority of results presented in Section 3 are obtained by reprocessing simulation output that were analyzed in previous studies utilizing histogram reweighting.[22,25] New simulation results are provided for n-hexane, 2-methylpropane, 2,2-dimethylpropane, 2,2,4-trimethylhexane, 2,3-dimethylbutane, 2,3,4-trimethylpentane, 2,2,3,3-tetramethylbutane, and cyclohexane. All simulations are performed using GPU optimized Monte Carlo (GOMC) with Grand Canonical Monte Carlo (GCMC), where the chemical potential (μ), volume (V), and temperature (T) are constant.

A series of nine simulations are performed, two in the vapor phase, six in the liquid phase, and one near critical which acts as the "bridge" between the vapor and liquid phases. A low-density (less than twenty molecules) initial configuration is utilized for the vapor phase simulations, while the bridge and liquid phase simulations are initialized with a high-density (around 200 molecules) configuration. The system volume is the same for each simulation, but varies somewhat between compounds. The prescribed chemical potentials and temperatures for the branched alkanes are the same as those utilized in Mick et al.[22] The $\mu - T$ values for n-hexane and cyclohexane are determined in this study. All state points are reported in Supporting Information.

The equilibration stage for each GCMC simulation consists of 2×10^7 Monte Carlo steps (MCS). The production stage is 4×10^7 MCS for vapor simulations and 2.5×10^7 MCS for the liquid and "bridge" simulations. Snapshots (i.e., number of molecules, internal energy, and optionally the xyz coordinates) are stored every 200 MCS to reduce the correlation between sequential configurations. Thus, the total number of snapshots (N_{snaps}) is 2×10^5 for vapor simulations and 1.25×10^5 for liquid and "bridge" simulations.

8

The type of Monte Carlo move implemented for each step is selected randomly with a 20%, 10%, and 70% probability of performing a displacement, rotation, and particle swap move, respectively. The move probabilities are slightly different for cyclohexane, namely, 30%, 10%, 40%, and 20% for displacement, rotation, particle swap, and crank-shaft moves, respectively.

Four different applications for MBAR are demonstrated in this study, where slightly different types of simulation output are required. First, we demonstrate how MBAR yields consistent results to those previously reported using histogram reweighting. The standard simulation output is used in this application, namely, a 2x$K_{\mathrm{snaps}}^{\mathrm{tot}}$ array containing the number of molecules and the internal energy for all $K_{\mathrm{snaps}}^{\mathrm{tot}}$ snapshots. Second, we demonstrate how these same data can be used with MBAR to predict VLE properties when performing ϵ-scaling. Third, we investigate how well MBAR can predict VLE for force field j from configurations sampled with force field i. In this case, a 3x$K_{\mathrm{snaps}}^{\mathrm{tot}}$ array is required, where the additional column is the internal energy computed with force field j. Fourth, we demonstrate how storing basis functions is a computationally efficient method for predicting VLE for multiple force fields that are unknown at runtime.

2.3 GCMC-MBAR compared with GCMC-HR

Converting the GCMC simulation output into phase coexistence properties requires significant post-processing through reweighting. Histogram reweighting (HR) and, more generally, configuration reweighting is an important tool in many fields of molecular simulation. In fact, it has long since been known that it is possible to estimate properties for state j by reweighting configurations that were sampled with state i.[1,26–28] For example, umbrella sampling simulations are often processed using the weighted histogram analysis method (WHAM) to compute free energy differences between states. WHAM (or HR) is essentially an approximation of MBAR and, therefore, MBAR should be favored

whenever a histogram-free approach is feasible.[29]

In this study, we implement MBAR through the *pymbar* package available in Python 2.7. Before demonstrating how to compute vapor-liquid coexistence with GCMC-MBAR, we review the traditional GCMC-HR approach. We also discuss the steps of this procedure that are the same for both GCMC-HR and GCMC-MBAR. We refer the interested reader to the literature for derivations and more detailed discussion of the GCMC-HR equations (cf. 1).

The HR equation to compute the ensemble average for a given observable (O) is

$$\langle O(\mu, \beta) \rangle = \sum_U \sum_N O \times Pr(N, U; \mu, \beta) \tag{7}$$

where $\langle \ldots \rangle$ denotes an ensemble average and $Pr(N, U; \mu, \beta)$ is the probability of observing N particles with internal energy U for a given chemical potential (μ) and inverse temperature ($\beta \equiv \frac{1}{k_B T}$, where k_B is the Boltzmann constant). The probability is obtained with HR using

$$Pr(N, U; \mu, \beta) = \frac{\sum_{i=1}^{R} Pr_i(N, U) \exp(-\beta U + \beta \mu N)}{\sum_{i=1}^{R} K_i \exp(-\beta_i U + \beta_i \mu_i N + C_i)} \tag{8}$$

where $Pr_i(N, U)$ is the probability of occurrence N particles in the simulation cell with total configurational energy in the vicinity of U, R is the number of runs (where the ith run corresponds to β_i and μ_i), K_i is the total number of observations ("snapshots") for run i (i.e., $K_i = \sum_{N,U} Pr_i(N, U)$), and C_i are the "constants" that are calculated with the relationship

$$C(\mu, \beta) = -\ln \sum_U \sum_N \frac{\sum_{i=1}^{R} Pr_i(N, U) \exp(-\beta U + \beta \mu N)}{\sum_{i=1}^{R} K_i \exp(-\beta_i U + \beta_i \mu_i N + C_i)} \tag{9}$$

where $C_i \equiv C(\mu_i, \beta_i)$.

Equations 7, 8, and 9 only allow for reweighting simulations at a different β and μ. By contrast, MBAR can also be applied to reweight simulations for different force field parameters (θ). The analogous MBAR equation to Equation 7 is

$$\langle O(\theta, \mu, \beta)\rangle = \sum_{n=1}^{K_{\text{snaps}}^{\text{tot}}} O(\boldsymbol{x}_n, N_n; \theta, \mu, \beta) \times W_n(\theta, \mu, \beta) \tag{10}$$

where $\boldsymbol{x}_n, N_n$ are configurations sampled from $i = 1 \ldots R$ simulations at inverse temperature (β_i), chemical potential (μ_i), and force field parameters (θ_i). $W_n(\theta, \beta, \mu)$ is the weight of the nth configuration in a simulation with arbitrary μ, β, and θ. W_n is computed with the following expression (analogous to Equation 8)

$$W_n(\theta, \beta, \mu) = \frac{\exp[\hat{f}(\theta, \beta, \mu) - u(\boldsymbol{x}_n, N_n; \theta, \beta, \mu)]}{\sum\limits_{i=1}^{R} K_i \exp[\hat{f}(\theta_i, \beta_i, \mu_i) - u(\boldsymbol{x}_n, N_n; \theta_i, \beta_i, \mu_i)]} \tag{11}$$

where $\hat{f}(\theta, \beta, \mu)$ is the reduced free energy, K_i are the total number of snapshots from the ith run, and $u(\boldsymbol{x}_n, N_n; \theta, \beta, \mu)$ is the reduced potential energy evaluated with θ, β, and μ for configuration $\boldsymbol{x}_n, N_n$. For the grand canonical ensemble, $u(\boldsymbol{x}_n, N_n; \theta, \beta, \mu) = \beta U(\boldsymbol{x}_n; \theta) - \beta \mu N_n$. The reduced free energy is computed with an expression analgous to Equation 9

$$\hat{f}(\theta, \beta, \mu) = -\ln \sum_{n=1}^{K_{\text{snaps}}^{\text{tot}}} \frac{\exp[-u(\boldsymbol{x}_n, N_n; \theta, \beta, \mu)]}{\sum\limits_{i=1}^{R} K_i \exp[\hat{f}(\theta_i, \beta_i, \mu_i) - u(\boldsymbol{x}_n, N_n; \theta_i, \beta_i, \mu_i)]} \tag{12}$$

where $K_{\text{snaps}}^{\text{tot}} = \sum_i K_i$ is the total number of snapshots for all R runs.

Both HR and MBAR require solving a system of $R - 1$ nonlinear equations for self-consistency (Equations 8 and 9 for HR and Equations 11 and 12 for MBAR). Specifically, initial guesses for C_i (HR) or $\hat{f}$ (MBAR) are updated iteratively until convergence is achieved for the respective equations. There is provably only one solution, so as long as

certain criteria are met that will be discussed below. Thus, although a range of different solver methods exist, the only difference is efficiency and numerical stability.

A key advantage of MBAR over HR is that by changing from a sum over histograms to a sum over snapshots, we are free to perform simulations with other conditions besides μ and β. For example, we can carry out simulations at different force field parameters θ. In the histogram context, we cannot easily separate out samples in the same U histogram that were performed with different force field parameters. If we perform sums over samples, we can reevaluate the configuration with a range of different parameters for a relatively small expense.

However, if all R simulations are performed using a single reference force field (θ_{ref}) and W_n and $\hat{f}$ are only computed for $\theta = \theta_i = \theta_{\mathrm{ref}}$, the θ dependence of Equations 10, 11, and 12 is removed. In this case, these two sets of equations (HR: Equations 7, 8, and 9, MBAR: Equations 10, 11, and 12) can be seen as equivalent in the limit of infinitesimal histogram bin widths. In the zero bin width limit, no histogram contains more than 1 snapshot and, therefore, U and N for each histogram can be taken to be the $U(\boldsymbol{x}_n)$ and N_n of the single observation in that histogram, while histograms with no particles can be omitted. Thus, $Pr_i(N, U)$ is either 1 or 0, and the sum over all histograms becomes a sum over snapshots conducted in all R simulation runs. Equations 9 and 8 then reduce to Equations 12 and 11, respectively.

For both HR and MBAR, the pressure is computed from

$$P = \frac{k_{\mathrm{B}}T}{V} \ln \Xi + B \tag{13}$$

where Ξ is the grand partition function and B is an additive constant. For HR $\ln \Xi$ is proportional to C while for MBAR $\ln \Xi$ is proportional to $\hat{f}$. Therefore, the HR pressure

expression is

$$P(\mu_i, \beta_i) = C(\mu_i, \beta_i) + B \tag{14}$$

while the MBAR pressure expression is

$$P(\theta, \mu_i, \beta_i) = \hat{f}(\theta_i, \mu_i, \beta_i) + B \tag{15}$$

For both HR and MBAR, B is determined by fitting a straight-line to $\ln \Xi$ with respect to N at very low densities. At these low densities, the system is assumed to behave as an ideal gas and, therefore, the slope is unity and $B = \frac{k_{\mathrm{B}} T b}{V}$, where b is the y-intercept from the straight-line regression.

The saturated vapor pressure $(P_{\mathrm{vap}}^{\mathrm{sat}})$ is computed with Equations 14 (HR) or 15 (MBAR) at the saturation temperature (T^{sat}) and saturation chemical potential (μ^{sat}), where μ^{sat} is determined by equating the pressures in the vapor and liquid phases at a fixed value of T^{sat}. The two phases are integrated separately by dividing the snapshots into low and high density regimes. For example, the equality of pressures is satisfied for HR when

$$\sum_{U} \sum_{N > N_{\mathrm{c}}} Pr(N, U; \mu^{\mathrm{sat}}, \beta^{\mathrm{sat}}) = \sum_{U} \sum_{N < N_{\mathrm{c}}} Pr(N, U; \mu^{\mathrm{sat}}, \beta^{\mathrm{sat}}) \tag{16}$$

where N_{c} is an estimate for the number of molecules at the critical density, which serves to distinguish between snapshots that are in the vapor or liquid phases. The analogous MBAR equation is

$$\sum_{n=1}^{K_{\mathrm{snaps}}^{\mathrm{tot}}} W_n(\theta, \beta, \mu) H_{\mathrm{vap}}(N_n) = \sum_{n=1}^{K_{\mathrm{snaps}}^{\mathrm{tot}}} W_n(\theta, \beta, \mu) H_{\mathrm{liq}}(N_n) \tag{17}$$

where N_n is the number of molecules in the nth snapshot and H_{vap} and H_{liq} are the Heav-

iside step functions for the vapor and liquid phases, respectively, such that

$$H_{\text{vap}}(N) = \begin{cases} 1 & N \le N_{\text{c}} \\ 0 & N > N_{\text{c}} \end{cases} \tag{18}$$

$$H_{\text{liq}}(N) = \begin{cases} 0 & N \le N_{\text{c}} \\ 1 & N > N_{\text{c}} \end{cases} \tag{19}$$

By solving Equations 16 (HR) or 17 (MBAR) for μ^{sat}, the vapor and liquid saturation densities and energies ($\rho_{\text{liq}}^{\text{sat}}$, $\rho_{\text{vap}}^{\text{sat}}$, $U_{\text{liq}}^{\text{sat}}$, and $U_{\text{vap}}^{\text{sat}}$) are also computed with a modified version of Equations 7 (HR) or 10 (MBAR) where only snapshots from the desired phase are included in the weighted average. For example, when computing $\rho_{\text{liq}}^{\text{sat}}$ and $U_{\text{liq}}^{\text{sat}}$, the double summation in Equation 7 (HR) is performed only for $N > N_{\text{c}}$ and the integrand of Equation 10 (MBAR) is multiplied by $H_{\text{liq}}(N_n)$. Having computed the pressure, internal energies, and densities, the enthalpy of vaporization is calculated with

$$\Delta H_{\text{v}} = \bar{U}_{\text{vap}}^{\text{sat}} - \bar{U}_{\text{liq}}^{\text{sat}} + P_{\text{vap}}^{\text{sat}}(\bar{V}_{\text{vap}}^{\text{sat}} - \bar{V}_{\text{liq}}^{\text{sat}}) \tag{20}$$

where $\bar{U}$ and $\bar{V}$ denote molar energy and molar volume, respectively.

The performance of HR and MBAR depends primarily on good phase space overlap. For HR, good overlap means that the different sets of T and μ generate configurations that are representative of the vapor and liquid phases at T^{sat} and μ^{sat}. For MBAR, an additional requirement is that the configurations sampled with θ_{ref} also represent feasible configurations for θ_{rr}.[12,30] The amount of overlap can be quantified by the number of

effective snapshots $(K_{\text{snaps}}^{\text{eff}})$,[?] using Kish's formula:

$$K_{\text{snaps}}^{\text{eff}} = \frac{\left(\sum_n W_n\right)^2}{\sum_n W_n^2} \tag{21}$$

which reduces to $K_{\text{snaps}}^{\text{eff}} = (\sum_n W_n^2)^{-1}$ when the weights are normalized. This has the property that when the weights are equal, $K_{\text{snaps}}^{\text{eff}} = K_{\text{snaps}}^{\text{tot}}$, when all but one weight is negligible, $K_{\text{snaps}}^{\text{eff}} \approx 1$, and behaves appropriately for intermediate cases. Messerly et al. proposed a heuristic stating that MBAR-ITIC is reliable when $K_{\text{snaps}}^{\text{eff}} > 50$.

2.4 Basis functions

When applying MBAR to different non-bonded parameter sets, $\theta_{\text{rr}} \neq \theta_{\text{ref}}$, it is necessary to recompute the internal energy for each snapshot. Millions of snapshots are required for precise estimates of $\rho_{\text{liq}}^{\text{sat}}$, $\rho_{\text{vap}}^{\text{sat}}$, $P_{\text{vap}}^{\text{sat}}$, and ΔH_{v}. The naive approach is to store the molecular configurations at each snapshot and then recompute the energies using θ_{rr}. Although the "rerun" step is orders of magnitude faster than performing direct GCMC simulations with θ_{rr}, the naive approach is memory intensive and computationally expensive. Fortunately, basis functions can greatly accelerate the energy recomputation step.[12,30]

Basis functions can be applied whenever the energy can be linearly separated. For example, the Mie λ-6 non-bonded energy is separated into a repulsive and attractive term that can be expressed as

$$u^{\text{nb}}(C_6, C_\lambda; r) = C_\lambda r^{-\lambda} - C_6 r^{-6} \tag{22}$$

where C_6 and C_λ are proportional to $\epsilon\sigma^6$ and $\epsilon\sigma^\lambda$, respectively. Therefore, the total non-bonded energy (U^{nb}) is simply

$$U^{\text{nb}}(C_6, C_\lambda; r) = C_\lambda \sum r^{-\lambda} - C_6 \sum r^{-6} \tag{23}$$

where $\sum r^{-\lambda}$ is the repulsive basis function, $\sum r^{-6}$ is the attractive basis function and, for simplicity, $\sum$ denotes a sum over all unique pairwise interactions.

For a given λ, the total internal energy can be recomputed for any value of ϵ and σ. As C_λ depends on λ, a separate repulsive basis function is required for each value of λ. Rather than storing configurations (which must be full-precision for reliable "rerun" results) and recomputing r for each unique pairwise interaction, basis functions only require storing two floating point values ($\sum r^{-\lambda}$ and $\sum r^{-6}$). Therefore, basis functions greatly reduce both the memory storage load as well as the computational cost to recompute the energy for each snapshot.

2.5 ϵ-scaling

Recently, Weidler and Gross proposed "individualized," i.e., compound-specific, parameter sets for compounds which contain large amounts of experimental data.[19] To avoid overfitting, a one-dimensional optimization is employed which scales ϵ for all united-atom sites while not adjusting σ or λ.

This requires applying GCMC-MBAR with $\epsilon_{\mathrm{rr}} = \psi \times \epsilon_{\mathrm{ref}}$ while $\sigma_{\mathrm{rr}} = \sigma_{\mathrm{ref}}$ and $\lambda_{\mathrm{rr}} = \lambda_{\mathrm{ref}}$.

GCMC-MBAR is ideally suited for this "ϵ-scaling" approach for at least two reasons. First, as mentioned previously, MBAR is most reliable when extrapolating in ϵ rather than σ and/or λ. Second, the rate-limiting step for GCMC-MBAR is recomputing the configurational energies for a different force field. Furthermore, storing millions of configuration ("snapshots") is highly memory intensive. While basis functions (see Section 2.4) alleviate the additional computational cost and reduce the memory load, ϵ-scaling does not require storing/recomputing configurations or basis functions. Instead, the energies for each snapshot are simply multiplied by the ϵ-scaling parameter.

3   Results

In this section, we present results from several different applications of GCMC-MBAR. First, we compute vapor-liquid coexistence properties in the case where the force field parameters do not change, i.e., $\theta_{\text{rr}} = \theta_{\text{ref}}$. Second, we perform a one-dimensional optimization in the ϵ-scaling parameter, ψ. Third, we determine the reliability of GCMC-MBAR when $\theta_{\text{rr}} \neq \theta_{\text{ref}}$ for different literature force fields. Fourth, we demonstrate how GCMC-MBAR can be applied to obtain new Mie λ-6 parameters for cyclohexane.

3.1   Constant θ

Section 2.3 demonstrated that MBAR and HR are mathematically equivalent in the limit of zero bin width and when $\theta_{\text{rr}} = \theta_{\text{ref}}$. Figure 1 provides numerical validation that GCMC-MBAR and GCMC-HR yield indistinguishable vapor-liquid coexistence properties. The evidence for this conclusion is that the median percent deviation is approximately zero and that the largest deviations are within a few percent. The percent deviations shown in Figure 1 are averaged over the 31 branched alkanes studied by Mick et al. and the 11 alkynes studied by Barhaghi et al. The GCMC-HR values were not recomputed in this study but were taken from the literature.[22,25] The GCMC-MBAR values were computed using a subset of the raw simulation data from Mick et al. and Barhaghi et al. Specifically, snapshots from only a single replicate simulation were used for the GCMC-MBAR analysis, while the GCMC-HR values reported by Mick et al. and Barhaghi et al. utilized five replicate simulations.

3.2 ϵ-scaling

Reference 19 proposes an ϵ-scaling approach for converting transferable parameters (namely, TAMie) into individualized (compound-specific) parameters (iTAMie). The phi-
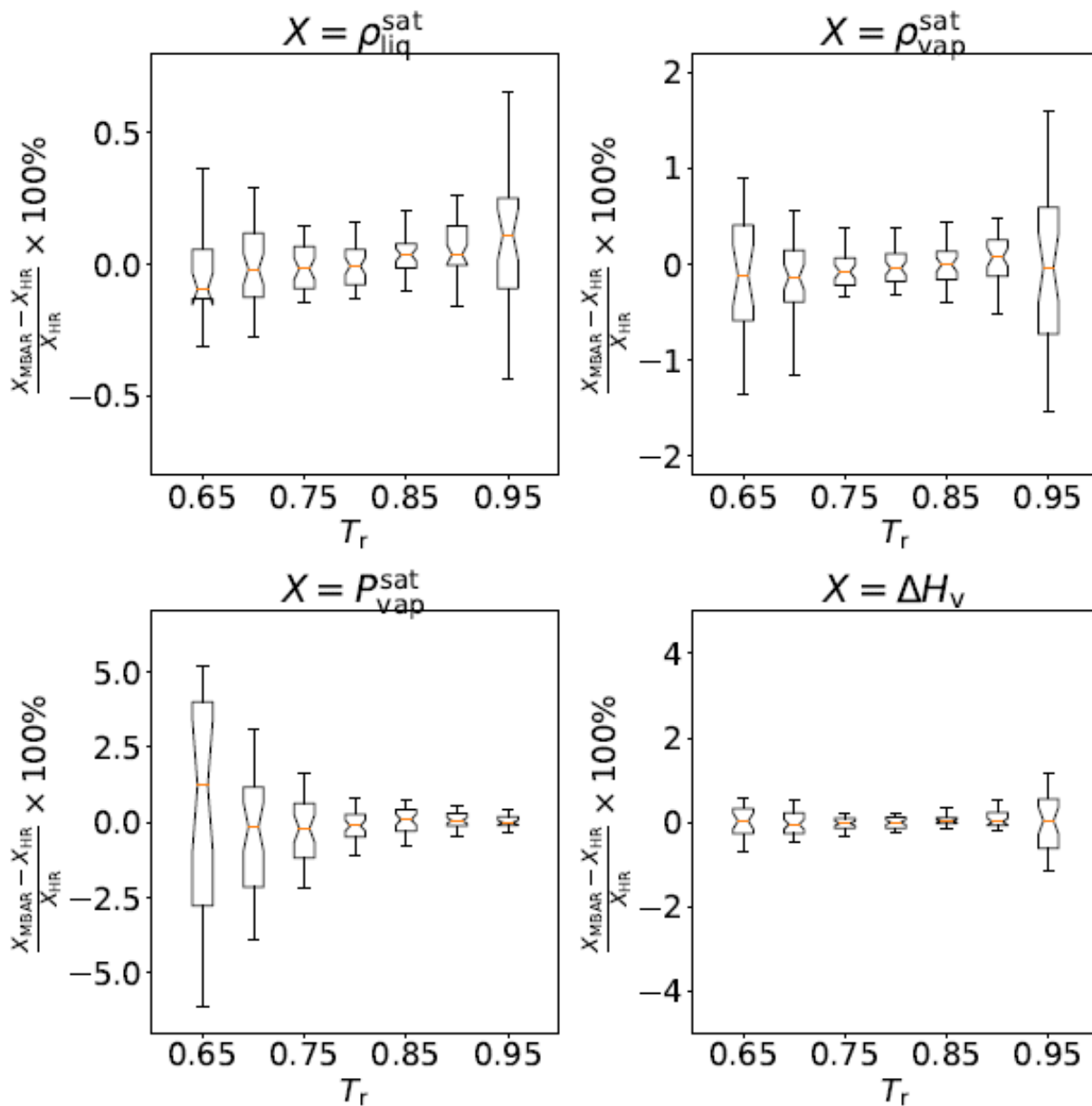
Figure 1: Percent deviations between coexistence properties computed using histogram reweighting (HR) and Multistate Bennett Acceptance Ratio (MBAR). Top-left, top-right, bottom-left, and bottom-right panels correspond to saturated liquid density, saturated vapor density, saturated vapor pressure, and enthalpy of vaporization, respectively. Boxes depict the first and third quartiles while whiskers represent the range that contains 95% of the data.

losophy for individualized parameters is that some compounds have sufficient reliable experimental data to refine the force field parameters for a specific molecule. However,

refitting all non-bonded parameters simultaneously would likely lead to an underspecified optimization and, thus, an overfit parameter set. For this reason, Weidler et al. optimize a single adjustable parameter (ψ) that scales all the ϵ values according to

$$\epsilon_{ii}^{\mathrm{ind}} = \psi \epsilon_{ii}^{\mathrm{tran}} \tag{24}$$

where $\epsilon_{ii}^{\mathrm{ind}}$ is the individualized ϵ value for united-atom ii, $\epsilon_{ii}^{\mathrm{tran}}$ is the corresponding transferable ϵ value, and ψ is a constant value for a given compound.

Figure 2 presents the ϵ-scaling results for 8 branched alkanes and 11 alkynes using the MiPPE force field as the initial force field. For consistency with the original MiPPE optimization, we use the same objective function for the branched alkanes and alkynes of Mick et al. and Barhaghi et al., respectively. Furthermore, the target values are computed with pseudo-experimental correlations. The alkyne correlations are from the Design Institute for Physical Properties (DIPPR) while the branched alkane correlations are from the National Institute of Standards and Technology (NIST) Reference Fluid Properties (REFPROP) database.

Figure 2 shows that the alkynes require a greater degree of scaling than the branched alkanes. Weigler et al. tend to characterize the individualization as being useful when the scaling is greater than 0.4% (i.e., $|1 - \psi| > 0.004$). With this rationale, of the branched alkanes only 3-methylpentane merits ϵ-scaling for MiPPE-SL. Similarly, the TAMie force field also found $\psi \approx 1$ for all branched alkanes, except 3-methylpentane. Although ψ values for iTAMie were not reported for alkynes, the largest ψ value for olefins, ethers, and ketones was ≈ 1.01. A truly transferable force field should have $\psi \approx 1$ for all compounds. Therefore, the transferability of the MiPPE force field appears to be slightly poorer for 2-pentyne and 2-hexyne, which have an optimized $\psi > 1.01$. It is also interesting that only 3 out of 19 compounds require $\psi < 1$. Thus, the well-depths appear to be slightly under-

estimated by the MiPPE force field. By contrast, this trend was not observed in Reference 19 for TAMie.
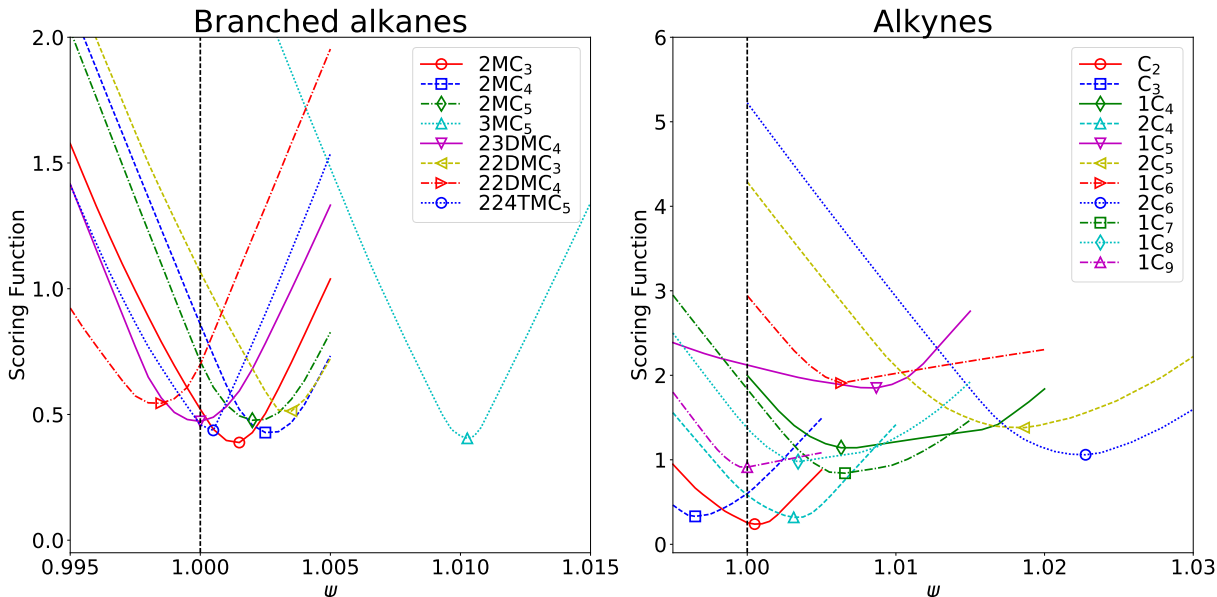

Figure 2: One dimensional optimization with ϵ-scaling (ψ) of MiPPE-SL for select branched alkanes (left) and alkynes (right). Open symbols correspond to the optimal ψ value for a given compound.

3.3 $\epsilon_{\mathrm{ref}} \neq \epsilon_{\mathrm{rr}}$, $\sigma_{\mathrm{ref}} \neq \sigma_{\mathrm{rr}}$, and $\lambda_{\mathrm{ref}} \neq \lambda_{\mathrm{rr}}$

A more demanding test of GCMC-MBAR than ϵ-scaling is to vary several non-bonded parameters simultaneously, including σ and λ. Because it is not possible to visualize a parameter space of greater than two dimensions, we perform this analysis of GCMC-MBAR using the TraPPE, NERD, MiPPE-gen, and MiPPE-SL force fields. Specifically, we utilize GCMC-MBAR to predict coexistence properties for the NERD and MiPPE-SL force fields using configurations sampled from TraPPE and MiPPE-gen, respectively (see Figure 3). We also use GCMC-MBAR to predict coexistence properties of the TraPPE force field by sampling configurations with MiPPE-gen, and vice versa (see Figure 4).

Note that all three non-bonded parameters (ϵ, σ, and λ) for all four united-atom types

20

(CH$_3$, CH$_2$, CH, and C) are different between the TraPPE and MiPPE-gen force fields. The TraPPE and NERD ϵ and σ values are different for all four united-atom types while $\lambda = 12$ for both force fields. The MiPPE-gen and MiPPE-SL force fields only differ in the ϵ and/or σ values for the CH and C sites . Specifically, the 2-methylpropane parameters are identical except for σ_{CH}, the 2,2-dimethylpropane parameters are the same except for ϵ_{C}, and three parameters are different for 2,2,4-trimethylpentane (ϵ_{CH}, σ_{CH}, and σ_{C}). However, the difference in ϵ and σ values for MiPPE-gen and MiPPE-SL is significantly smaller than that between TraPPE and NERD.

Figures 3 and 4 compare the GCMC-MBAR predicted values for $\theta_{\text{rr}} \neq \theta_{\text{ref}}$ to those for $\theta_{\text{rr}} = \theta_{\text{ref}}$. Figure 3 contains $\lambda_{\text{rr}} = \lambda_{\text{ref}}$ while Figure 4 corresponds to $\lambda_{\text{rr}} \neq \lambda_{\text{ref}}$. As observed in Figures 3 and 4, MBAR is extremely reliable at predicting vapor phase properties ($\rho_{\text{vap}}^{\text{sat}}$ and $P_{\text{vap}}^{\text{sat}}$) while it is less reliable for liquid phase properties ($\rho_{\text{liq}}^{\text{sat}}$ and ΔH_{v}, which depends on both phases). In particular, note that the $\rho_{\text{liq}}^{\text{sat}}$ estimates in Figure 4 are sporadic and unreliable. This undesirable behavior can be explained by the low number of effective snapshots in the liquid phase.

Figure 5 demonstrates that $K_{\text{snaps}}^{\text{eff}}$ is typically much greater in the vapor phase than in the liquid phase. Messerly et al. report that MBAR-ITIC is reliable if $K_{\text{snaps}}^{\text{eff}} > 50$. Applying this heuristic to GCMC-MBAR helps qualify why the liquid properties are poorly estimated in some systems while the vapor properties are much more accurate. Specifically, $K_{\text{snaps}}^{\text{eff}}$ is less than 50 in the liquid phase when $\lambda_{\text{rr}} \neq \lambda_{\text{ref}}$, while is much greater in the liquid phase than the vapor phase. if the overlap between systems is sufficient for MBAR to be reliable. is

The poor overlap when varying λ is consistent with the MBAR-ITIC results.[12] However, GCMC-MBAR provides considerable improvement in predicting $P_{\text{vap}}^{\text{sat}}$ compared to MBAR-ITIC. For this reason, we recommend reducing the $\rho_{\text{liq}}^{\text{sat}}$ weight in the scoring function when varying λ. The degree to which the weight is reduced should depend on the

number of effective samples.

1. We validate that MBAR and HR are statistically indistinguishable with sufficient data by re-analyzing the simulation results of Mick et al. and Barhaghi et al. utilizing MBAR

2. Epsilon scaling for all the compounds that Mohammad has U and N values for (branched alkanes and alkynes) and which have good experimental data

3. We estimate MiPPE generalized and NERD VLE from TraPPE simulations, MiPPE S/L from MiPPE generalized, and TraPPE from MiPPE generalized

4. For $\lambda_{\mathrm{ref}} = 12$ and $\lambda_{\mathrm{rr}} = 16$, MBAR-GCMC predicts vapor density, vapor pressure, and heat of vaporization more accurately than liquid density

5. For $\lambda_{\mathrm{ref}} = 12$ and $\lambda_{\mathrm{rr}} = 12$, i.e., computing NERD from TraPPE simulations, MBAR-GCMC predicts all four properties accurately

6. We present how basis functions allow for rapid computation of wide range of parameter sets:

   (a) 2-methylpropane

   (b) 2,2-dimethylpropane

   (c) cyclopentane or cyclohexane

7. We provide supporting information with basis functions for several branched alkanes with TraPPE and MiPPE force fields

3.4   Figures

1. Percent deviation between MBAR and HR results for rholiq, rhovap, Psat, and DeltaHv

2. Comparison between MBAR bootstrapping and analytical uncertainties and HR uncertainties (?)

3. Scaling of epsilon post-simulation for branched alkanes and alkynes

4. Prediction of VLE for $\lambda_{\text{ref}} \neq \lambda_{\text{rr}}$

5. Prediction of VLE for $\lambda_{\text{ref}} = \lambda_{\text{rr}}$

6. Two-D scans of scoring functions for $\epsilon-\sigma$ of CH3 (a) and CH (b) for 2-methylpropane

7. Two-D scans of scoring functions for $\epsilon-\sigma$ of CH3 (a) and C (b) for 2,2-dimethylpropane

8. Two-D scans of scoring functions for $\epsilon - \sigma$ of CH2 for cyclopentane or cyclohexane (reference is TraPPE)

4 Discussion/Limitations/Future work

As ITIC is more reliable at near-triple-point conditions, MBAR-ITIC and MBAR-GCMC can be combined to cover most temperatures that span the vapor-liquid coexistence curve.

1. We recommend that future GCMC-VLE studies report the snapshots of N and U and/or basis functions to recompute U as this allows for future force field optimization

2. Improvements are possible with multiple θ or simulating a range of μ values

5 Conclusions

6 Acknowledgments

References

(1) Panagiotopoulos, A. Z. Monte Carlo methods for phase equilibria of fluids. *Journal of Physics: Condensed Matter* **2000**, *12*, R25.

(2) Fern, J. T.; Keffer, D. J.; Steele, W. V. Measuring Coexisting Densities from a Two-Phase Molecular Dynamics Simulation by Voronoi Tessellations. *The Journal of Physical Chemistry B* **2007**, *111*, 3469–3475.

(3) Razavi, S. M.; Messerly, R. A.; Elliott, J. R. Coexistence Calculation Using the Isothermal-Isochoric Integration Method. **2018**, *Pending publication.*

(4) Martin, M. G.; Siepmann, J. I. Transferable potentials for phase equilibria. 1. United-atom description of n-alkanes. *J. Phys. Chem. B* **1998**, *102*, 2569–2577.

(5) Hemmen, A.; Gross, J. Transferable Anisotropic United-Atom Force Field Based on the Mie Potential for Phase Equilibrium Calculations: n-Alkanes and n-Olefins. *J. Phys. Chem. B* **2015**, *119*, 11695–11707.

(6) Potoff, J. J.; Bernard-Brunel, D. A. Mie Potentials for Phase Equilibria Calculations: Applications to Alkanes and Perfluoroalkanes. *J. Phys. Chem. B* **2009**, *113*, 14725–14731.

(7) Ungerer, P.; Beauvais, C.; Delhommelle, J.; Boutin, A.; Rousseau, B.; Fuchs, A. H. Optimization of the anisotropic united atoms intermolecular potential for n-alkanes. *J. Chem. Phys.* **2000**, *112*, 5499–5510.

(8) Messerly, R. A.; KnottsIV, T. A.; Wilding, W. V. Uncertainty quantification and propagation of errors of the Lennard-Jones 12-6 parameters for n-alkanes. *J. Chem. Phys.* **2017**, *146*, 194110.

(9) Chodera, J. D.; Swope, W. C.; Pitera, J. W.; Seok, C.; Dill, K. A. Use of the weighted histogram analysis method for the analysis of simulated and parallel tempering simulations. *J. Chem. Theory Comput.* **2007**, *3*, 26–41.

(10) Shirts, M. R.; Chodera, J. D. Statistically optimal analysis of samples from multiple equilibrium states. *J. Chem. Phys.* **2008**, *129*, 124105.

(11) Boulougouris, G. C.; Peristeras, L. D.; Economou, I. G.; Theodorou, D. N. Predicting fluid phase equilibrium via histogram reweighting with Gibbs ensemble Monte Carlo simulations. *The Journal of Supercritical Fluids* **2010**, *55*, 503 – 509, 100th year Anniversary of van der Waals' Nobel Lecture.

(12) Messerly, R. A.; Razavi, S. M.; Shirts, M. R. Configuration-Sampling-Based Surrogate Models for Rapid Parameterization of Non-Bonded Interactions. *Journal of Chemical Theory and Computation* **2018**, *14*, 3144–3162.

(13) Messerly, R. A.; Shirts, M. R.; Kazakov, A. F. Uncertainty quantification confirms unreliable extrapolation toward high pressures for united-atom Mie λ-6 force field. *The Journal of Chemical Physics* **2018**, *149*, 114109.

(14) Razavi, S. M. Optimization of a Transferable Shifted Force Field for Interfaces and Inhomogenous Fluids using Thermodynamic Integration. M.Sc. thesis, The University of Akron, 2016.

(15) Kiyohara, K.; Spyriouni, T.; Gubbins, K. E.; Panagiotopoulos, A. Z. Thermodynamic scaling Gibbs ensemble Monte Carlo: a new method for determination of phase coexistence properties of fluids. *Molecular Physics* **1996**, *89*, 965–974.

(16) Errington, J. R.; Panagiotopoulos, A. Z. Phase equilibria of the modified Buckingham exponential-6 potential from Hamiltonian scaling grand canonical Monte Carlo. *The Journal of Chemical Physics* **1998**, *109*, 1093–1100.

(17) Errington, J. R.; Panagiotopoulos, A. Z. A new intermolecular potential model for the n-alkane homologous series. *J. Phys. Chem. B* **1999**, *103*, 6314–6322.

(18) Errington, J. R.; Panagiotopoulos, A. Z. New intermolecular potential models for benzene and cyclohexane. *The Journal of Chemical Physics* **1999**, *111*, 9731–9738.

(19) Weidler, D.; Gross, J. Individualized force fields for alkanes, olefins, ethers and ketones based on the transferable anisotropic Mie potential. *Fluid Phase Equilibria* **2018**,

(20) Martin, M. G.; Siepmann, J. I. Novel Configurational-Bias Monte Carlo Method for Branched Molecules. Transferable Potentials for Phase Equilibria. 2. United-Atom Description of Branched Alkanes. *The Journal of Physical Chemistry B* **1999**, *103*, 4508–4517.

(21) Shah, M. S.; Siepmann, J. I.; Tsapatsis, M. Transferable potentials for phase equilibria. Improved united-atom description of ethane and ethylene. *AIChE J.* **2017**, *63*, 5098–5110.

(22) Mick, J. R.; Soroush Barhaghi, M.; Jackman, B.; Schwiebert, L.; Potoff, J. J. Optimized Mie Potentials for Phase Equilibria: Application to Branched Alkanes. *J. Chem. Eng. Data* **2017**, *62*, 1806–1818.

(23) Nath, S. K.; Escobedo, F. A.; de Pablo, J. J. On the simulation of vapor-liquid equilibria for alkanes. *J. Chem. Phys.* **1998**, *108*, 9905–9911.

(24) Allen, M. P.; Tildesley, D. J. *Computer simulation of liquids*; Clarendon Press ; Oxford University Press: Oxford England New York, 1987; pp xix, 385 p.

(25) Barhaghi, M. S.; Mick, J. R.; Potoff, J. J. Optimised Mie potentials for phase equilibria: application to alkynes. *Molecular Physics* **2017**, *115*, 1378–1388.

(26) McDonald, I. R.; Singer, K. Machine Calculation of Thermodynamic Properties of a Simple Fluid at Supercritical Temperatures. *The Journal of Chemical Physics* **1967**, *47*, 4766–4772.

(27) Card, D. N.; Valleau, J. P. Monte Carlo Study of the Thermodynamics of Electrolyte Solutions. *The Journal of Chemical Physics* **1970**, *52*, 6232–6240.

(28) Wood, W. W. Monte Carlo Calculations for Hard Disks in the IsothermalâĂŘIsobaric Ensemble. *The Journal of Chemical Physics* **1968**, *48*, 415–434.

(29) Duarte Ramos Matos, G.; Kyu, D. Y.; Loeffler, H. H.; Chodera, J. D.; Shirts, M. R.; Mobley, D. L. Approaches for Calculating Solvation Free Energies and Enthalpies Demonstrated with an Update of the FreeSolv Database. *Journal of Chemical & Engineering Data* **2017**, *62*, 1559–1569.

(30) Naden, L. N.; Shirts, M. R. Rapid Computation of Thermodynamic Properties Over Multidimensional Nonbonded Parameter Spaces using Adaptive Multistate Reweighting. *J. Chem. Theory Comput.* **2016**, *12*, 1806–1823.

7   Supporting Information

7.1   MBAR VLE estimates

Provide tables of MBAR estimates

7.2   Basis functions

1. Validation that basis functions give accurate energies

7.3   Raw data

1. Comparison of 2-D histograms for TraPPE and MiPPE. MBAR overlap, possible? Probably not without rerunning the simulations.
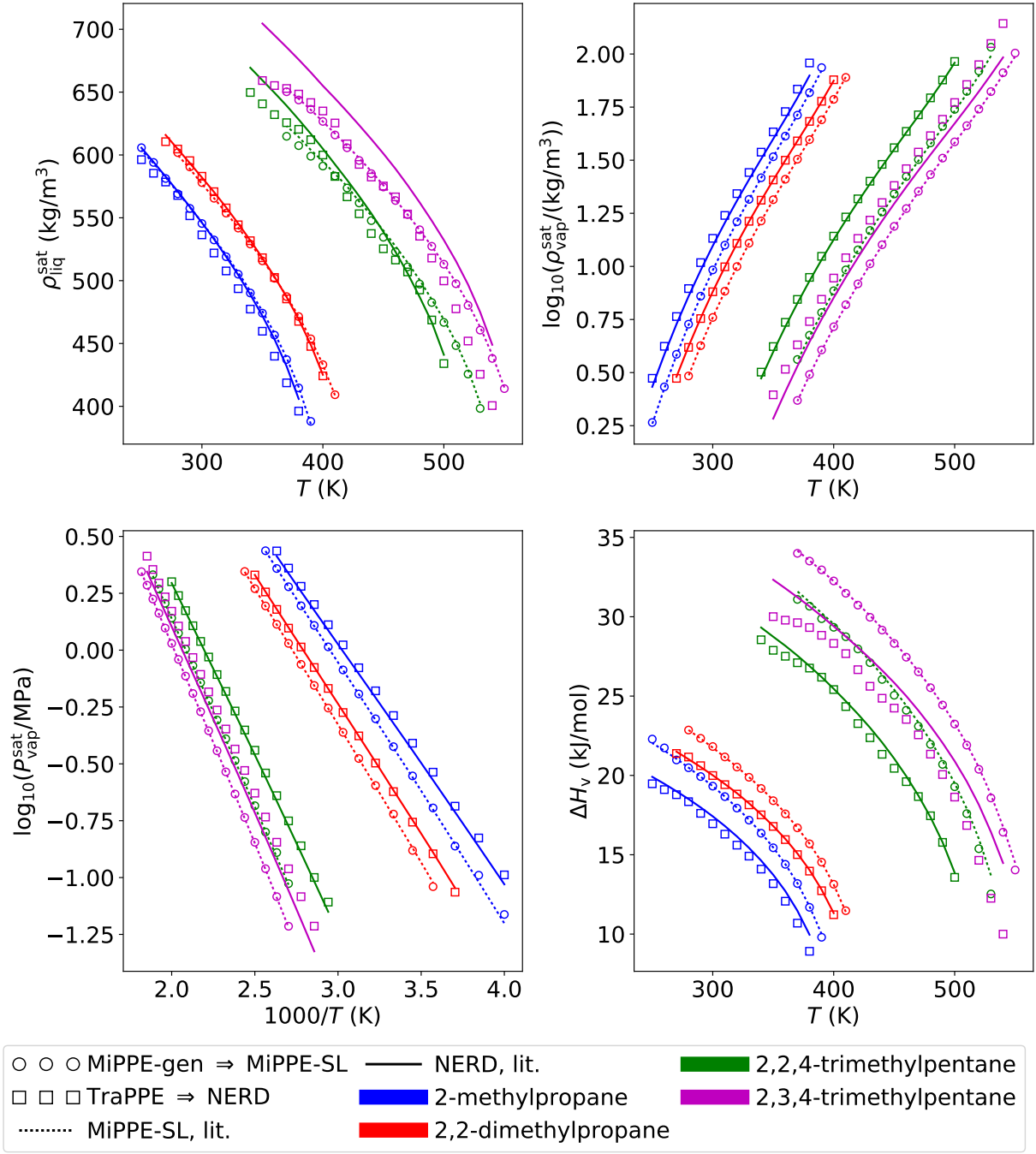
Figure 3: Comparison between MBAR-GCMC estimates (symbols, $\theta_{rr} \neq \theta_{ref}$) and MBAR-HR literature values (lines) with a constant repulsive exponent, i.e., $\lambda_{rr} = \lambda_{ref}$. MBAR-GCMC estimates for the NERD and MiPPE-SL force fields are computed using configurations sampled from TraPPE and MiPPE-gen, respectively. Top-left, top-right, bottom-left, and bottom-right panels correspond to saturated liquid density, saturated vapor density, saturated vapor pressure, and enthalpy of vaporization, respectively.
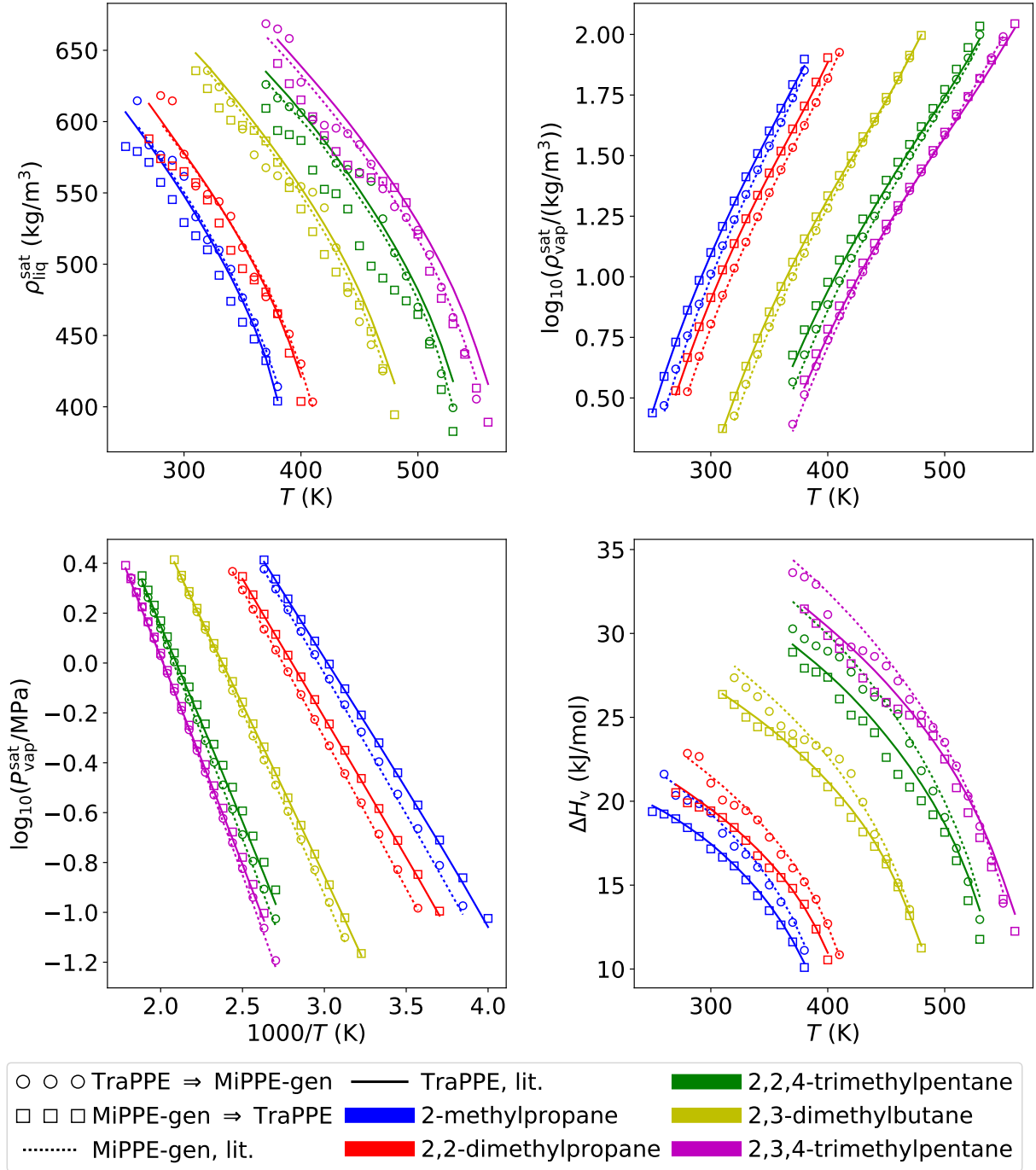
Figure 4: Comparison between MBAR-GCMC estimates (symbols, $\theta_{\mathrm{rr}} \neq \theta_{\mathrm{ref}}$) and MBAR-HR literature values (lines) with a non-constant repulsive exponent, i.e., $\lambda_{\mathrm{rr}} \neq \lambda_{\mathrm{ref}}$. MBAR-GCMC estimates for the TraPPE force field are computed using configurations sampled from MiPPE-gen, and vice versa. Top-left, top-right, bottom-left, and bottom-right panels correspond to saturated liquid density, saturated vapor density, saturated vapor pressure, and enthalpy of vaporization, respectively.
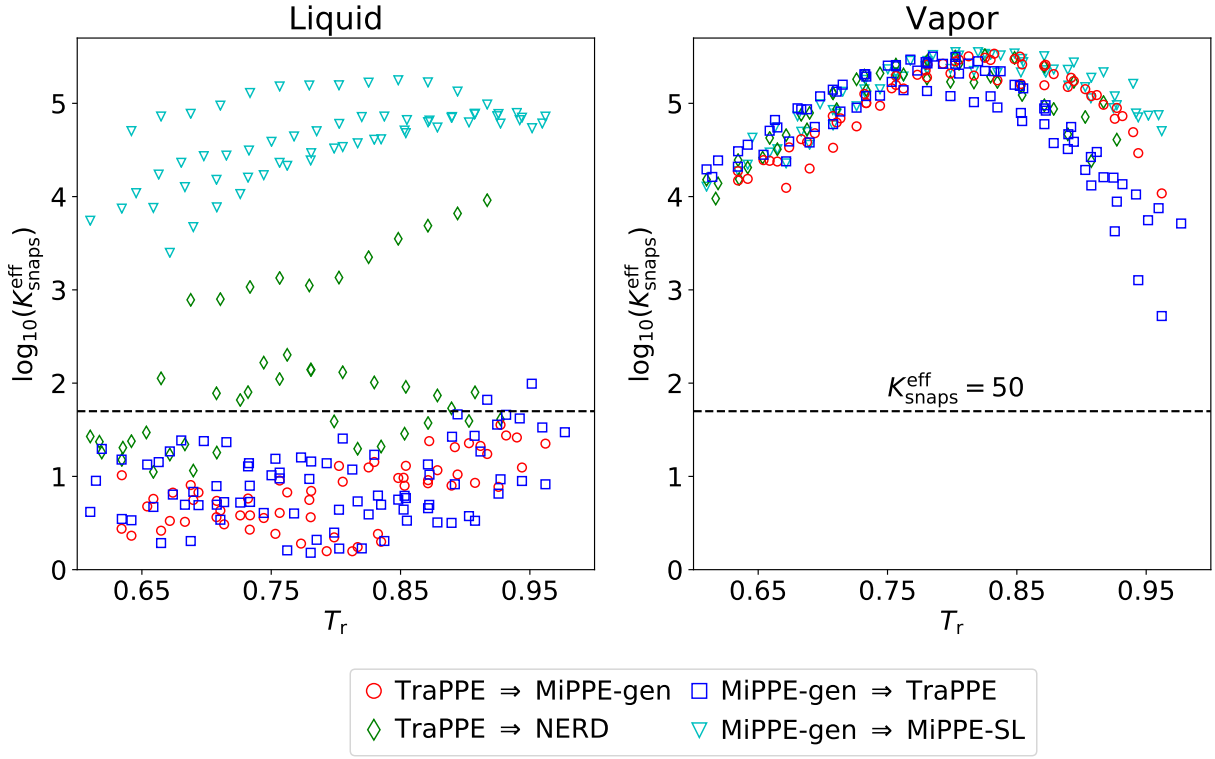
Figure 5: Number of effective snapshots ($K_{\text{snaps}}^{\text{eff}}$) in the liquid (left panel) and vapor (right panel) phases.